



# Bio-inspired design, modeling, and 3D printing of lattice-based scale model scooter decks

Naser Namvar<sup>1</sup> · Ilya Moloukzadeh<sup>1</sup> · Ali Zolfagharian<sup>2</sup> · Frédéric Demoly<sup>3</sup> · Mahdi Bodaghi<sup>4</sup> 

Received: 4 November 2022 / Accepted: 26 February 2023  
© The Author(s) 2023

## Abstract

This research aims at enhancing the performance of scale-model scooter decks by investigating various architected cellular metamaterial and bio-inspired core structure designs, such as honeycomb, tetrachiral, re-entrant, arrowhead, and star-shaped arrangements. An initial effort is made toward the design and rapid prototyping of small-scale deck with a uniform honeycomb core structure. More specifically, polylactic acid is utilized to fabricate complex structures via fused filament fabrication technique. Investigation is then focused on its mechanical performance, such as its bending properties obtained through a three-point bending test. Simulations are also conducted with different core configurations using a geometrically non-linear finite element method which is implemented. Experiments are carried out to verify the numerical results. After validation, various patterns are modeled, and eventually, it is observed that the functionally graded arrowhead structure has the best bending resistance, compared to other bio-inspired and mechanical metamaterial structures. At a constant force of 845 N, the functionally graded arrowhead design lowers the deflection in the middle of the scale model of scooter deck by up to 14.7%, compared to the uniform arrowhead structure. Furthermore, comparing the tetrachiral and functionally graded arrowhead configurations at a constant force, a 30% reduction in central deflection was observed. Due to the lack of similar results and designs in the specialized literature, this work could potentially advance the state-of-the-art scooter core designs and provide designers with architectures that could enhance the performance and safety of scooters.

**Keywords** Metamaterial · Scooters · Bio-inspired design · Lattice · 3D printing · FEM

## Nomenclature

AM Additive manufacturing  
CAD Computer-aided design  
CFD Computational fluid dynamic  
FEM Finite element method  
FG Functionally graded  
FFF Fused filament fabrication  
NPR Negative Poisson's ratio

PLA Polylactic acid  
ZPR Zero Poisson's ratio

## 1 Introduction

In recent years, modeling and optimizing mechanical design solutions have become indispensable strategies for addressing technical issues in sports equipment. Investigating these methods could have a broad range of advantages, such as cost-effectiveness, injury control, safety promotion, weight reduction, and improved performance. According to these methods, Shimoyama et al. improved the design of a sports shoe sole by implementing a finite element method (FEM) to reduce the sole's weight [1]. Caravaggi et al. designed an innovative device that protects the cervical spine and subsequently keeps the athlete's neck in its safe physiological range [2]. Guidimetla et al. studied the hydrodynamic performance of three- and four-fin surfboard configurations using the computational fluid dynamics (CFD) method [3]. Results revealed that the maximum lift coefficient for the

✉ Mahdi Bodaghi  
mahdi.bodaghi@ntu.ac.uk

<sup>1</sup> Department of Mechanical Engineering, University of Tabriz, Tabriz, Iran

<sup>2</sup> School of Engineering, Deakin University, Geelong, Victoria 3216, Australia

<sup>3</sup> ICB UMR 6303 CNRS, Belfort-Montbéliard University of Technology, UTBM, 90010 Belfort Cedex, France

<sup>4</sup> Department of Engineering, School of Science and Technology, Nottingham Trent University, Nottingham NG11 8NS, UK

three-fin configuration occurs at a smaller angle of incidence than for the four-fin design. Meanwhile, the maximum lift amount was similar for both designs under the operating conditions. Furthermore, by implementing a composite foam with a column/matrix composite configuration for head protection application based on a FEM, Mosleh et al. indicated that rotational acceleration and velocity of the head form can remarkably be minimized during indirect impact [4]. Sakellariou et al. maximized the lift-per-drag ratio by employing genetic algorithms coupled with CFD to optimize a surfboard fin shape [5]. According to their findings, the optimized fin design increased the lift-to-drag ratio by nearly 62%. In addition, Penta et al. developed a mesh-free Element Galerkin method to study the impact behavior of ethylene-vinyl acetate protective foam mats [6]. The final modeling approach was influential in reducing head injury risk as a reliable computational approach.

Scooters have proliferated rapidly as an economical personal mode of transportation. They have gained massive attention due to their low manufacturing cost, eco-friendliness, and greater convenience in parking and moving compared to other private transportation means. They are designed in a variety of shapes, sizes, and types, including kick-scooters, motor-scooters, and e-scooters. In such a product category, as decks are developed with aspect ratios ranging from 5:1 to 3:1. Although there are some differences between the different types of scooters, the deck is the most critical part since it bears the rider's weight. In addition, even though the speed of kick-scooter barely reaches 16 km/h, some e-scooters can travel faster than 40 km/h. For instance, a rider, weighing 80 kg and riding on a flat surface, may apply approximately a force of 785 N to a conventional deck. An impact force of 2,354 N would be exerted on the deck if an 80 kg rider jumped off a ramp at a height of about 1 m [7]. Hence, this can make this part vulnerable in some circumstances, resulting in deck fractures and increasing the chance of accidents. To tackle these concerns, more bio-friendly and lightweight materials with highly rigid structures can be developed. It is worth noting that reducing the total weight of the scooter is a vital factor since; in the long run, this remarkably diminishes fuel consumption as well as fuel expenditures [7]. A study conducted by Aizpuru et al. about scooter injuries in the USA showed that approximately 32,400 motorized scooter injuries occurred from 2013 to 2017 [8]. Furthermore, not only did the estimated incidence not change distinctly over this period of time, but also scooter injuries for millennials saw an exponential increase of 77%.

Among the lightweight structures developed to increase mechanical performance, sandwich structures are multilayered composite structures comprising three layers, i.e., two thin skin-layer facings on each side and a low-density core between them. Employing low-density cores in panels and

boards has several benefits, such as minimizing the chance of breakage, maintaining a high strength-to-weight ratio, improving stability, bending stiffness, and other mechanical properties [9, 10]. Platek et al. compared graded 3D printed structures fabricated by two different printing methods, including fused filament fabrication (FFF) and selective laser sintering (SLS) [11]. They concluded that there is a negative correlation between a structure's topology and its relative density versus energy absorption capacity. Compton et al. designed and fabricated different cellular composite structures and conducted compression tests to determine the cellular composite designs' behavior under crushing loads [12]. Among the geometric designs proposed in the literature, the bio-inspired honeycomb core structure has attracted tremendous attention compared to other core structures since it exhibited higher stiffness per weight [13].

Beyond layered structures, mechanical metamaterials refer to cellular artificial materials demonstrating eccentric properties which are not available in natural matter [14, 15]. Negative Poisson's ratio (NPR) [16, 17], tunable load-bearing capacity [18], and negative stiffness [19] are a few of these distinctive mechanical properties. Their extraordinary characteristics are derived from their structural geometries, not their chemical compositions [20]. The characteristics of mechanical metamaterials at larger sizes are determined by their small-scale geometry [21].

3D printing technology has been widely used for rapid prototyping, and its interest as a fabrication method has increased substantially across numerous disciplines [22]. This method enables the manufacturing of physical objects under computer control, generally through accumulating successive layers of materials laid down on each other. Despite being a new approach, this cutting-edge technology has demonstrated promising potential due to its advantages over traditional methods, such as cost and time reduction, as this procedure reduces machine, material, and labor expenses [23]. The current 3D printing industry is dominated by small-scale 3D printers (also known as desktop 3D printers) with an average estimated workspace of 200\*200 mm. Due to print capacity constraints, small-scale 3D printers are not always advantageous for industrial manufacturing. Increasing the scale of 3D printers provides significant benefits for manufacturing-focused businesses such as those in the automotive, aerospace, construction, marine, and agricultural sectors. In addition, sectors focusing on prototypes can still profit from large-scale 3D printers. Large-scale 3D printers have the potential to improve the industrial industry by enabling inexpensive, full-scale prototyping. They can decrease or eliminate the time and expense of building big molds and machining equipment. They can also possibly solve production difficulties caused by size scaling [22, 24, 25]. Industry and the manufacturing line can be revolutionized by 3D printing technology. Utilizing 3D printing

will accelerate production while cutting costs. The demand from consumers will also have more of an impact on manufacturing [26]. However, unlike more traditional methods like injection molding, where producing large volumes may be more cost-effective, 3D printing has a static cost. While 3D printing may have a lower initial investment than other manufacturing processes, once it is scaled up to mass-produce large volumes, the cost per unit does not decline as it would with injection molding. Rapid manufacturing is currently taking the place of rapid prototyping in FDM. New products, technology, and production processes must therefore be further developed [27]. Despite the fact that these disadvantage exist, generating complicated shapes and geometries and reducing waste to almost minimum during manufacturing process are the most significant advantages of this novel approach [28]. Recent years have witnessed studies regarding additive manufacturing (AM) in the area of sports markedly [] (see Fig. 1). Gately et al. fabricated surfboard fins from various composite materials using AM and employed CFD to calculate drag and turning forces [36]. Results indicated that surfboards' performance when containing 3D printed fins was akin to those with commercial fins. Park et al. designed and manufactured special rifle support for the sport of biathlon by combining 3D scanning, finite element analysis, topology optimization, and AM [37]. A 12.7% and 23–43% enhancement in the specific stiffness and structural safety in the printing direction were observed throughout the analyses performed on these structures. As compression tests were conducted to determine structural safety, the relative critical force showed a 40%

improvement over the original design. Soltani et al. analyzed additively manufactured on-water sports boards via different bio-inspired core structure designs [35]. They claimed that at 500 N, the functionally graded (FG) honeycomb design demonstrated 31% better bending resistance than the uniform honeycomb structure. Besides, a 97% decrease in the central deflection of the board was obtained at a fixed force of 400 N for FG honeycomb compared with the solid core board. Cazón-Martin et al. designed and fabricated shin pads for football players using AM [38]. A comparison of novel shin pads with traditional shin pads revealed a significant reduction in impact acceleration of between 42 and 68%. Furthermore, additively manufactured shin pads enhanced penetration from 13 to 32% while maintaining the same attenuation and contact times.

Although the literature review reveals that most of the previous studies [39, 40] have been directed to designing and modeling of scooter frames, no relevant literature has outlined a rule of thumb for fabricating scooter decks by applying various cellular cores via AM methods. In this work, we address the issue of fabricating a lightweight scale model of scooter deck with enhanced bending properties for the common scooters, by utilizing various metamaterial structural designs for the deck.

## 2 Materials and methods

### 2.1 Deck design with a uniform honeycomb sandwich structure

Mass reduction of all parts of the two-wheeled vehicle has become urgent to keep the overall vehicle mass within acceptable levels. The study by Koontz et al. suggested that lighter and less rigid vehicle designs could increase user maneuverability, convenience, and increase sustainability [41]. As a result, one of the most critical factors in the fabrication of scooters is identifying potential strategies that may cause a reduction of the weight. Among the materials used to fabricate scooter decks, aluminum is the most selected. On the other hand, polylactic acid (PLA) is a high-strength, lightweight, and high-modulus thermoplastic polymer that is more environmentally friendly than traditional materials used to fabricate scooter decks [42]. Utilizing scaling methodologies, a number of researchers [] have investigated scale effects in metals, composite materials, and sandwich structures. Prior research has offered an understanding of the scalability of load-bearing engineering structures, but 3D-printed structures have received insufficient investigation into their scaling implications. Predicting the mechanical performance of scaled 3D-printed structures, particularly for energy-absorbing purposes, requires additional research [4748]. Aziz et al. investigated the size implications on the flexural behavior



Fig. 1 Applications of 3D printing in sports equipment

of additively manufactured lattice structures using PLA in the sense of Buckingham's Pi theorem [49]. When comparing the quarter-size sample to its full-scale equivalent, the flexural strength improved by around 18%, which is not highly significant. However, after performing compression tests on scaled lattice structures, significant size effects were identified. Investigating the size effects on the mechanical response of the structures is somewhat outside the scope of this study and is suggested to be pursued in future research. Despite the PLA's low strength, this paper's primary goal is to compare flexural strength of various metamaterial structures. Thus with the aid of PLA as the parent material for the FFF method, sample scale models of scooter decks are fabricated, and compression tests are conducted. Other eco-friendly materials with a higher strength as the parent material and different additive manufacturing methods would be considered for further studies.

Herein, PLA, as one of the most commonly used materials in FFF, is used to manufacture the scale model of deck of a scooter. The intended scale model of scooter deck is divided into two sections. The first part is an upper shell, while the second is made up of a bottom cover merged with a lightweight core. The entire deck can be created using 3D printing in various shapes and patterns. Initially, a bio-inspired structure is designed for the deck's core. A beehive is comprised of a repeating pattern of hexagonal honeycomb patterns (see Fig. 2a), which inspires the geometric definition of the deck's core by a computer-aided design (CAD) software (CATIA® V5). The designed lattice structure and the 3D CAD scale model of deck components are shown in Figs. 2b and c, respectively.

Scooter decks with aspect ratios ranging from 5:1 to 3:1 are available on the market. One of the acceptable types of scooters are those with wide decks, 7" width, and as a commonly used example, they have a 3:1 aspect ratio. Here, a model of a scooter deck of a smaller size is developed on a scale of 3:1 compared to a real scooter deck. Moreover it is worth noticing that the dimensions shown in Fig. 3 are considered due to the bed size limitation of printer. The proposed honeycomb core deck and merged bottom shell are depicted in 2D with their respective dimensions in Fig. 3. The proposed scale model of deck has a 144 mm length and a 48 mm width. The hexagonal honeycomb design constitutes the deck's core and is replicated throughout the specimen. It is apparent from the detailed perspective that the hexagonals are prepared with walls that are 1 mm thick and 3 mm wide.

## 2.2 Materials and 3D printing

In order to characterize the mechanical properties of the printed PLA material, three dog-bone tensile samples are created using an FFF 3D printer (Ultimaker S3, the Netherlands) in accordance with the ASTM standard D638 (TYPE

IV) [50]. Specimens are tested under similar conditions to ensure the reliability of test results. The tensile test specimens are illustrated in Fig. 4a.

Generally, during the FFF process, raw filament materials enter in a liquefier chamber and turn into semi-molten plastic filament, which are selectively deposited through a nozzle on the heated platform in a layer-by-layer manner from bottom to top. In this study, PLA filaments (Recreus Inc., Elda, Spain) with a diameter of 2.85 mm are used. The nozzle and bed temperatures are set at 195°C and 60°C, respectively. The raster angle is fixed to be 0°, meaning that all the designs are filled in such a way that the printing raster is along the length direction. Eventually, a printing speed of 20 mm/s, an internal fill density of 100%, and a layer height of 0.2 mm are adjusted.

A uniaxial tensile test is carried out on tensile dog-bone samples using a Shimadzu AGS-X 50 kN (Kyoto, Kyoto Prefecture, Japan) testing machine. A constant crosshead speed of 1 mm/min and a load cell of 1 kN are considered, while the test is performed at room temperature. The strain rate is set at 0.050% s<sup>-1</sup> to guarantee that the test circumstances are quasi-static loading and that there is no viscosity dependency [51]. Figures 4a and b illustrate the tested specimen and the tensile experiment device, respectively.

The stress-strain curve of the tensile specimen is shown in Fig. 4c. All four dog-bone samples demonstrate identical diagrams with Young's modulus of 1.4 GPa. Poisson's ratio's value is also obtained 0.32. In addition, plasticity begins at 2.1% strain, and prior to breakdown, the PLA samples reach a maximum stress of 46.94 MPa. The material behavior may be classified as elasto-plastic due to the change in the slope of the stress-strain curve and residual deformation after unloading just before the breakdown.

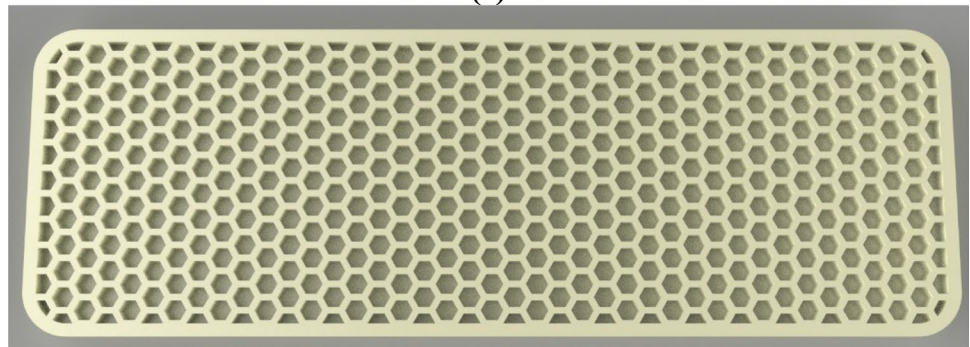
## 2.3 3D printing of the scale model of deck with a honeycomb core

In this step, using PLA filament, two parts of the scale model of deck are 3D printed individually. All process parameters are maintained as before, with the bed and nozzle temperatures, internal fill density, and print speed adjusted at 60°C, 195°C, 100%, and 20 mm/s, respectively. Figure 5a depicts the sections of the 3D-printed small-scale deck, whereas Fig. 5b illustrates the 3D-printed small-scale deck sections assembled with strong glue, Araldite 106 (AW106/HV953U). The specification of the adhesive is shown in Table 1. Since the main aim of the paper is to investigate the effect of various metamaterial structures on the bending resistance of scale model of scooter decks, examining the adhesive effects is beyond the aim of the paper and could be considered in future development efforts.

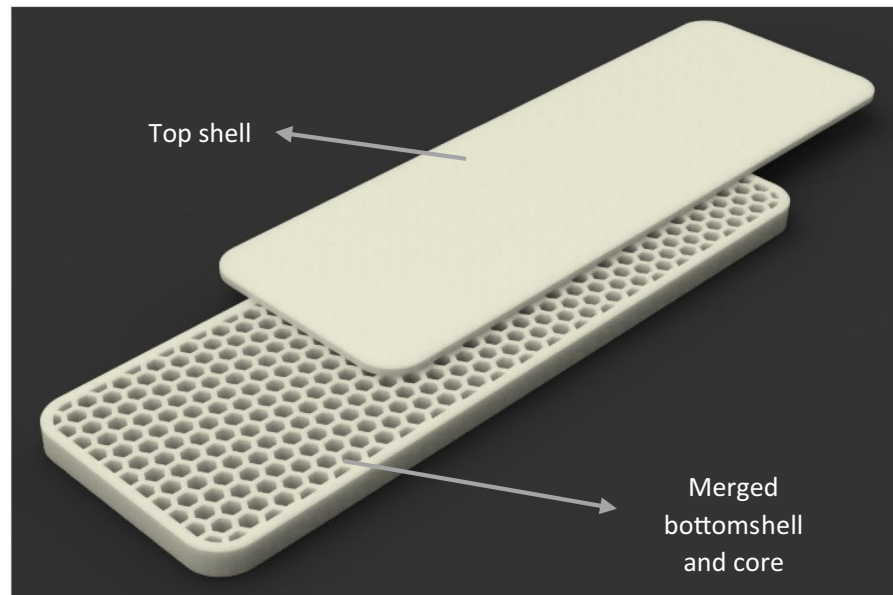
**Fig. 2** **a** Beehive, a common honeycomb structure in nature; **b** a small-scale deck designed with a honeycomb core pattern; **c** deck components: the upper shell and the assembled bottom shell with honeycomb core



(a)



(b)



(c)

#### 2.4 Experimental test of the small-scale deck with the uniform honeycomb core

While cruising on a scooter, two main forces exert stress on the vehicle's deck. A force is induced into the middle of the deck due to the weight of the rider's body. The second occurs when the rider pitches relative to the vehicle frame.

Since the rider stands in the center of the deck, as illustrated in Fig. 6a, the forces are primarily directed toward the middle, as similar as in the three-point bending test (see Fig. 6b). Over time, these stresses can damage the deck and cause it to fracture in the center.

Bending stresses generally induce breakage, so a mechanical three-point bending test could be suitable to assess the

**Fig. 3** 2D definition of the bio-inspired honeycomb lattice structure (dimensions are in mm)

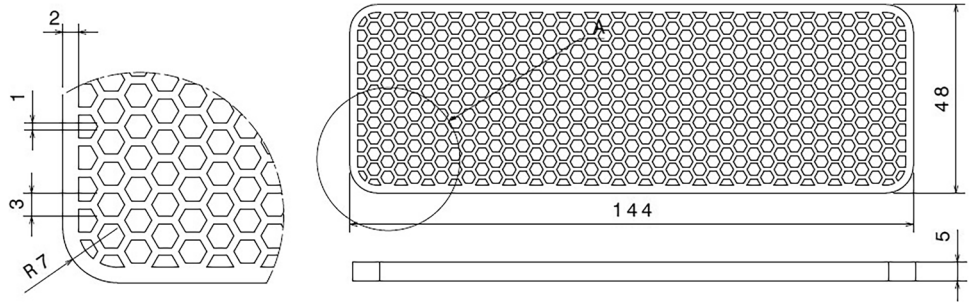
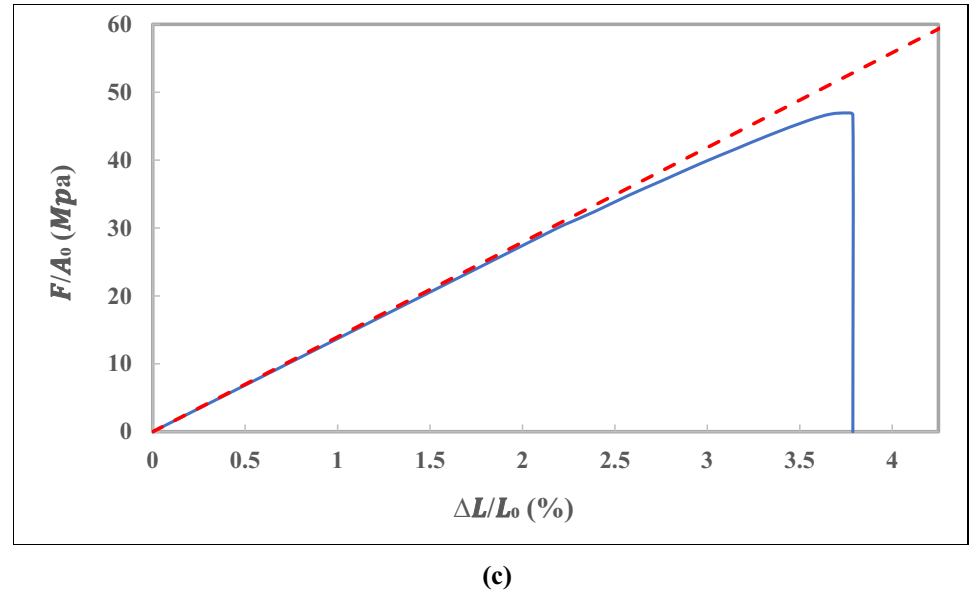
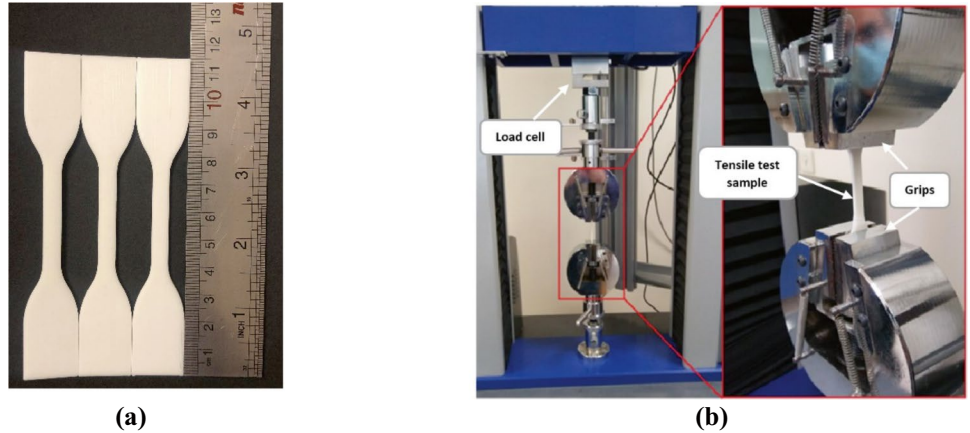


**Fig. 4** **a** Tensile test specimens; **b** Shimadzu AGS-X tensile testing machine; **c** stress-strain diagram of the 3D-printed PLA



deck's strength when subjected to such loads. The tests are run under worst-case scenario boundary conditions, which means that the force is applied at the center of the deck to ensure that the maximum deflection is determined. The work presented here focuses on characterizing the bending resistance behavior of different core structures under quasi-static loading condition. Systematic study of the fatigue mechanisms and dynamic loading would, however, require

extensive fatigue and loading-rate effect tests that are suggested to be pursued in future research. The three-point bending test is conducted on the 3D-printed scale model of deck with a uniform honeycomb core pattern. In order to perform the experiment, the gripper of the tensile test machine has to be replaced. Rather than using the upper grip, a loading nose is used to apply force to the middle of the sample. Furthermore, the lower grips of the machine

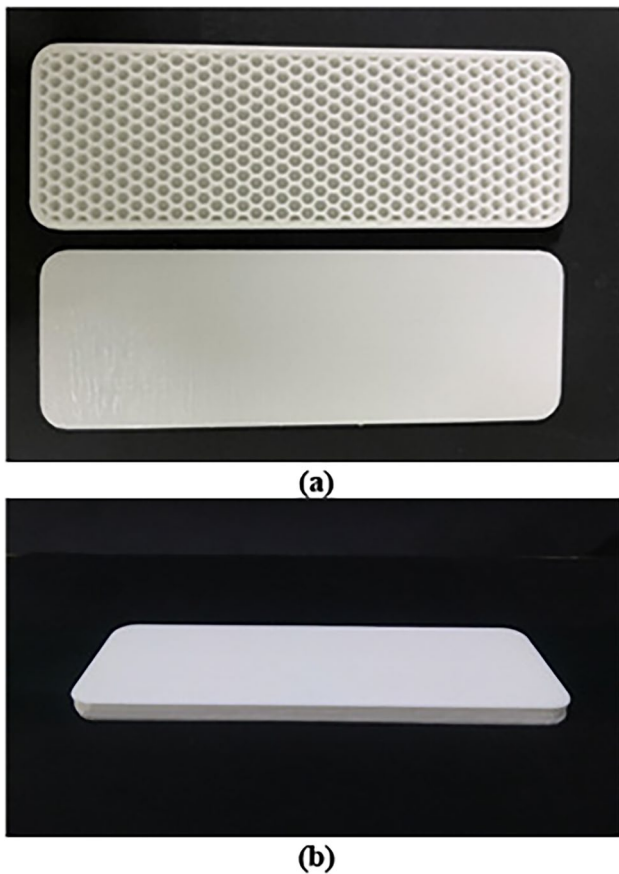


**Fig. 5** **a** Two 3D-printed parts of the small-scale deck; **b** two parts assembled with adhesive

are replaced by two supports to ensure the specimen is held tight. As seen in Fig. 7, the scale model deck is placed under the three-point bending test machine. The test is conducted at room temperature, with a constant crosshead speed of 1 mm/min and an 80 mm distance between two supports. Also, an experiment with controlled displacement was carried out to achieve a maximum deflection of 4 mm within the elastic range.

**2.5 FEM and experimental validation**

This section is dedicated to utilizing the FEM software package ANSYS, as a digital tool to numerically replicate mechanical behaviors of the scale model of scooter

deck with various designed core structures under three-point bending tests. Initially, the developed parts of the scale model deck, containing the top shell and merged bottom shell with the core, are transferred to ANSYS. It is noteworthy to mention that the linear elastic behavior and Young’s modulus of the PLA material are inputted into ANSYS according to the tensile test results, shown in Fig. 4c. A proper mesh generation as a critical part of the work is taken into consideration since the meshing elements must successfully cover the geometry thoroughly with good precision. In this regard, tetragonal elements are selected. In order to ensure that the simulation results are not mesh-dependent, a mesh sensitivity analysis is first conducted. For both the top and bottom shell, the total number of elements after convergence are 4061 and 34,123, respectively.

Each piece must be meshed separately to simulate ideal bonding between segments in the model. Thus, using the bonded contact at the interfaces of the top and merged bottom shell is essential. Since numerical results are supposed to be validated experimentally, the boundary conditions are the same as in the actual three-point bending experiment. Since decks are only functional when they are in the elastic regime, elastic phase properties of these structures are determined in this work. Rational design of mechanical metamaterials are utilized to explore and determine the structures that will not be plastically deformed subjected to the same load, which means they have higher strength in the elastic regime and simulations are maintained accordingly. Using the fixed boundary condition, two supports with a radius of 5 mm are fixed by 80 mm distance beneath the specimen, as shown in Fig. 8. Besides, a z-displacement of -4 mm is exerted on the loading nose. Afterward, a simulated three-point bending test is carried out on the designed scale model deck with a uniform honeycomb core structure to replicate the experiment.

Eventually, by means of three-point bending, a maximum deflection of 4 mm is obtained for the scale model of deck with a honeycomb core structure. Figure 9 demonstrates the von Mises stress contour, which, as expected, indicates that the maximum stress occurs in the middle of the deck. The highest stress is observed 28.919 MPa, which is sufficiently low to keep the scale model of deck in the ideal elastic region since the previously examined PLA material has a yield stress of 44 MPa.

**Table 1.** Specification of the adhesive and the hardener

Property	Araldite AW 106	Hardener HV 953 U	Mix
Color (Visual)	Neutral	Pale yellow	Pale yellow
Specific gravity	ca. 1.15	ca. 0.95	ca. 1.05
Viscosity at 25°C (Pa·s)	30-50	20-35	30-45
Pot life (100 gm at 25°C)	-	-	ca. 100 min

**Fig. 6 a** The most common situations of the rider's feet: when the rider's foot is placed in the middle of the deck, the maximum force is exerted, **b** three-point bending schematic.

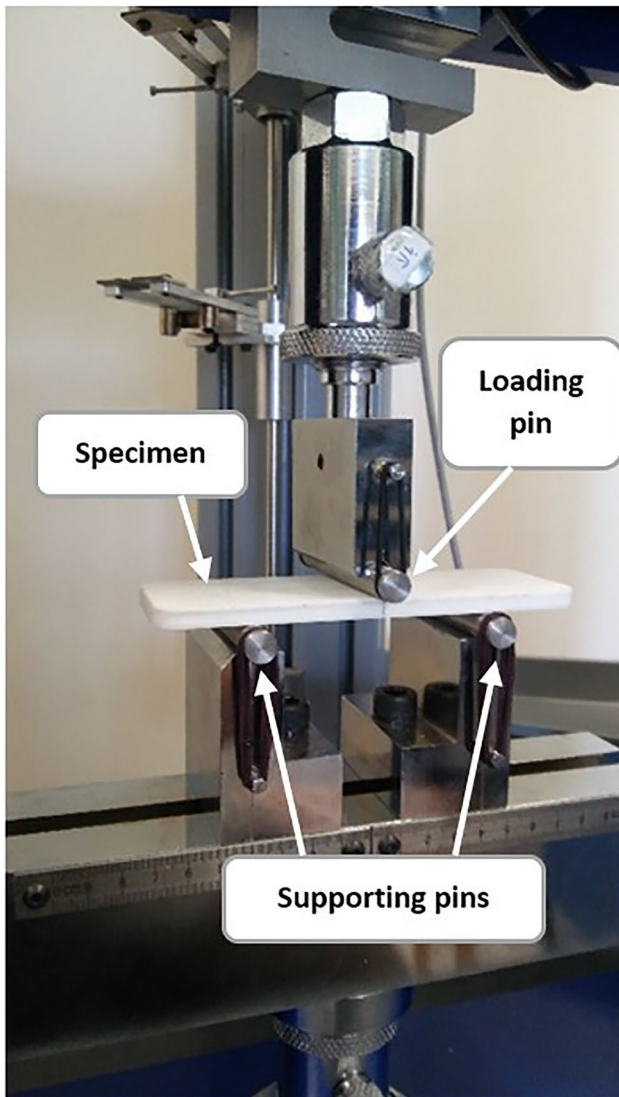
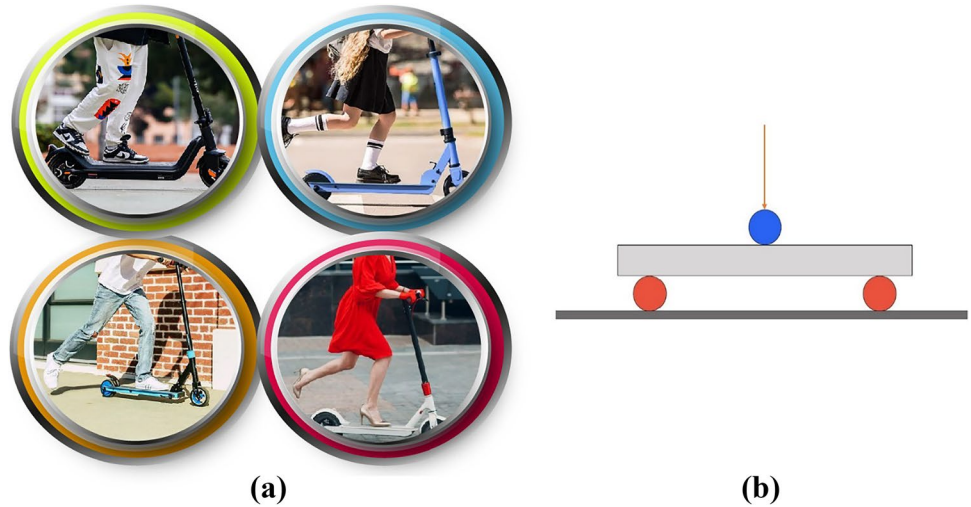


**Fig. 7** The scale model deck with a honeycomb structure core under the three-point bending test.

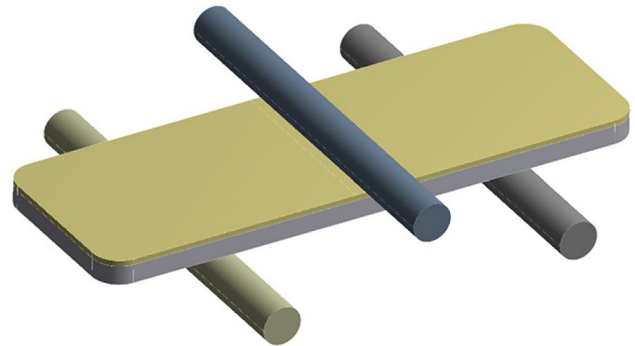


**Fig. 8** Boundary conditions of the FEM simulation

Figure 10 provides an illustration of force-deflection curves plotted for the experimental as well as the geometrically non-linear numerical results. It is found from the information supplied that the PLA scale model of deck manifests a linear elastic deformation of up to 700 N. Nevertheless, beyond which the material yields, plastic deformation occurs as a peak, approximately after 800 N. The non-linearity observed in the experiment between 700 and 800 N could be associated with the geometrical non-linearity in the linear elastic regime. It is evident that, from a design standpoint, slight elastic deformations up to stress values of around 800 N are acceptable. As can be seen, at the start of the deflection (less than 0.5 mm), the numerical results are in excellent agreement with the experimental results. However, the contrast between the numerical and experimental results is a bit boosted as the deflection grows. Figure 10 reveals that the FEM can accurately replicate the elastic behavior of the scale model of scooter deck up to a 4 mm deflection. It is seen that the FEM is able to replicate the switch in the elastic behavior from geometrical linearity to geometrical non-linearity that happens in the range of 700–800 N or 3–4 mm. Finally, it is observed that beyond 4 mm of deflection, the material experiences a plastic deformation that is not desired and could

**Fig. 9** von Mises stress contour (in MPa) of the scale model of scooter deck with the honeycomb lattice structure

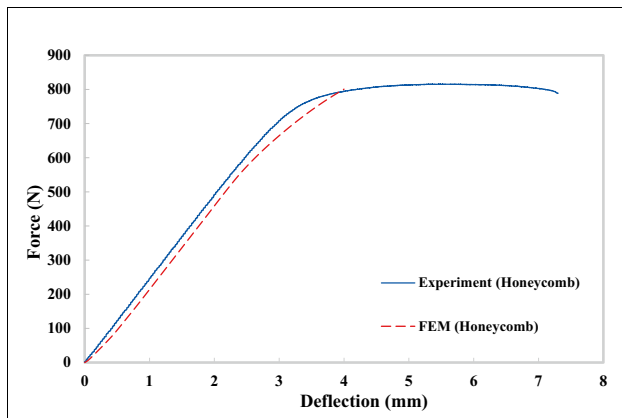
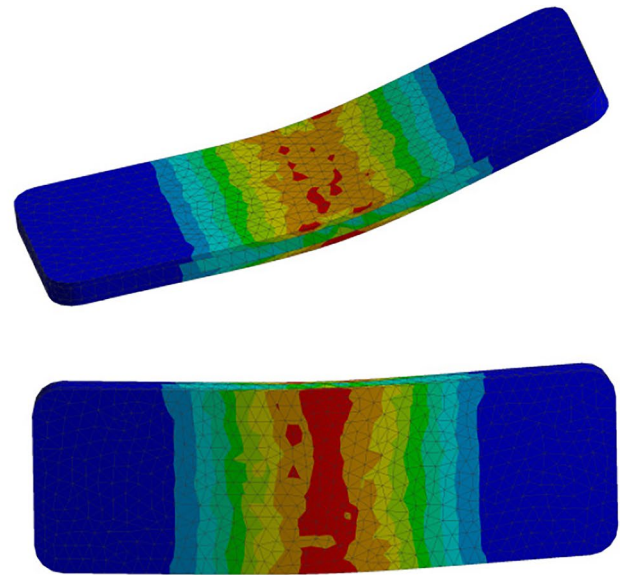
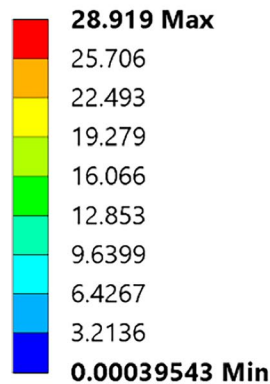


**Fig. 10** Comparison between numerical and experimental load-deflection responses of the honeycomb scale model of decks under the three-point bending test.

significantly affect the scooter integrity. In order to statistically elevate the data dispersion between the experimental results and FEM results, the error is calculated. The obtained error percentage is almost 5%, which is relatively low.

### 3 New design with results and discussion

#### 3.1 Design of core patterns

After validating the geometrically non-linear FEM model of the 3D-printed scale model of deck with the honeycomb core structure, several additional bio-inspired and metamaterial patterns are proposed for the core of the merged bottom shell. This section aims to determine which cellular lattice structure would reveal the highest value of bending resistance. Although all the designed scale model of decks have identical external frames,

the cores are represented by distinct patterns. In addition, the whole volume of the scale model of deck and upper frame geometry are kept constant. To accurately assess the mechanical properties of all configurations, it is vital to study them under similar circumstances; hence, all samples are designed with the same mass. All the cores weight 31 g, besides, the upper shells used in this paper for all the samples have equal mass. Various architected metamaterial and bio-inspired configurations like re-entrant, tetrachiral, star-shaped, arrowhead, and FG arrowhead cellular lattice structures are developed. All models have undergone a mesh convergence analysis to eliminate mesh sensitivity and establish the optimal element size and number for the FEM models. Likewise, calculating the maximum stresses of all decks with different core designs has shown that the highest stress is notably lower than the yield stress of the PLA material.

##### 3.1.1 Re-entrant structure

Among many auxetic architected metamaterial structures, re-entrant, presented by Almgren, has achieved much attraction and has been investigated broadly due to its great potential of energy absorption, adaptability, and capability to develop a high NPR [52]. These privileges have made this design a favored alternative for numerous applications [53]. Materials manufactured by 2D re-entrant pattern with high ductility demonstrate acceptable auxetic behaviors and load-carrying capability under static loading. In addition, they exhibit high stability and ductility under dynamic tensile or compressive loading [54]. According to the research conducted by Namvar et al., re-entrant auxetic structures exhibited a higher energy absorption capacity due to the unique deformation mechanics of unit cells [55].

As a result, this paper studies the bending performance of this metamaterial structure. The bottom shell of the scale model of deck designed with the re-entrant structure and the dimensions of the re-entrant unit cell are presented in Fig. 11a and b.

### 3.1.2 Tetrachiral structure

Chiral patterns pervade all around nature, commonly in natural plants and animals, such as right-handed and left-handed sea shells and helical goat horns, as depicted in Fig. 12a and

b. Prall and Lakes conducted a theoretical and experimental study about properties of chiral lattice structure [56]. It is called chiral when an object cannot be superposed to its mirror image by rotations and translations alone [57]. The design incorporates an in-plane NPR and a deformation mechanism that allows for high strains in the component material's elastic range [58]. Depending on the number of ligaments connected to the node ring, tetrachiral structure is one of the forms of chiral structure [59]. Qi et al. investigated the effects of geometric parameters on the crushing response of the tetrachiral lattice pattern [60]. An effective Poisson's ratio of the

**Fig. 11** **a** Re-entrant lattice core structure; **b** 2D definition with dimensions of the re-entrant unit cell

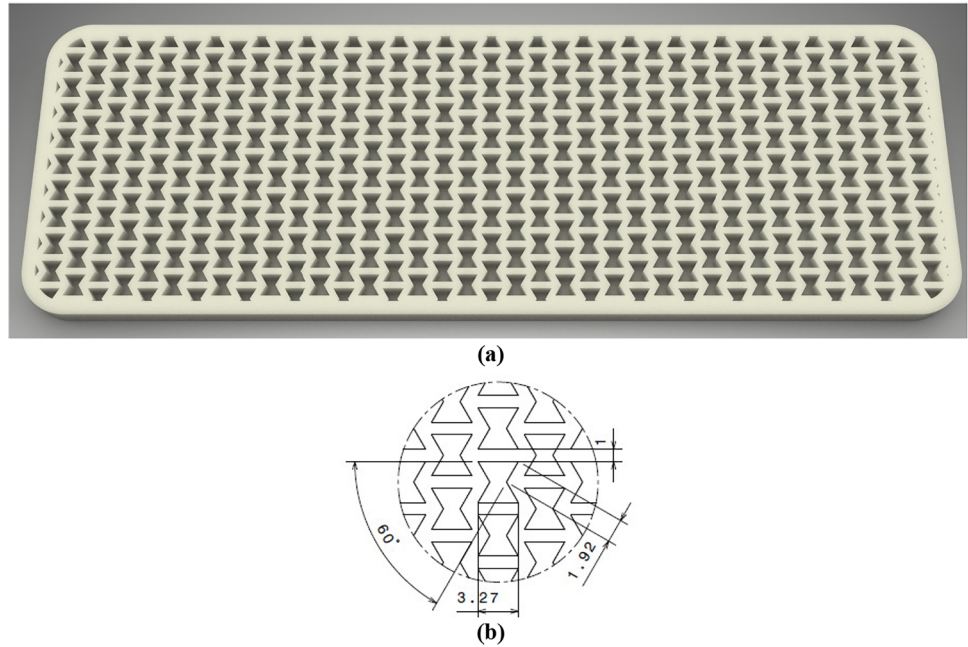
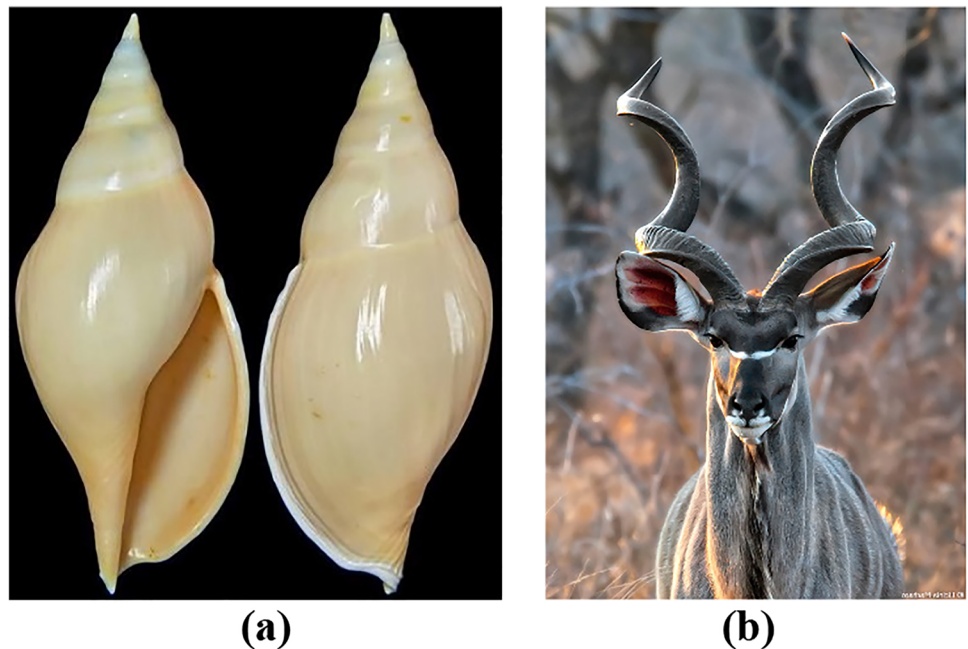


**Fig. 12** Chiral patterns in nature: **a** right-handed and left-handed sea shells; **b** helical goat horns



tetrachiral lattice structure was observed to vary with strain during quasi-static and dynamic in-plane crushing. Therefore, this functional bio-inspired design is applied to the scale model of scooter deck in this paper to investigate its bending capabilities. Figures 13a and b depict a comprehensive view of geometry and the dimensions of the tetrachiral pattern applied to the scale model of deck.

### 3.1.3 Star-shaped structure

The star-shaped structure can be formed by connecting 3, 4, and 6 arrows so that the arms of the arrows create stars [61]. Gong et al. investigated Young's in-plane shear modulus, Poisson's ratio, and transverse shear modulus of this novel design experimentally, analytically, and numerically [62]. In addition, Wenzhi et al. designed a novel 3D star-shaped zero Poisson's ratio (ZPR) with cubic symmetry based on a 2D star-shaped [63]. They investigated the

Young's modulus of the suggested novel pattern and presented an analytical model validated by FEM and experimental data. Their findings suggest that the ZPR effect is unaffected by the increase in the width-to-height ratio, which increases the material's rigidity. Consequently, this innovative metamaterial pattern has promising application prospects in several domains. In keeping with the widespread use of star-shaped patterns in nature (Fig. 14a and b), a 4-pointed star-shaped design is applied to the scale model of deck's core to investigate its bending properties. The stars are joined at the margins of this structure, as demonstrated in Fig. 15a. Besides, the dimensions of the lattice unit cell are depicted in Fig. 15b.

### 3.1.4 Arrowhead structure

An auxetic arrowhead design has been discovered by a numerical topology optimization method. Despite the

**Fig. 13** **a** Tetrachiral lattice core structure; **b** dimensions of the tetrachiral unit cell

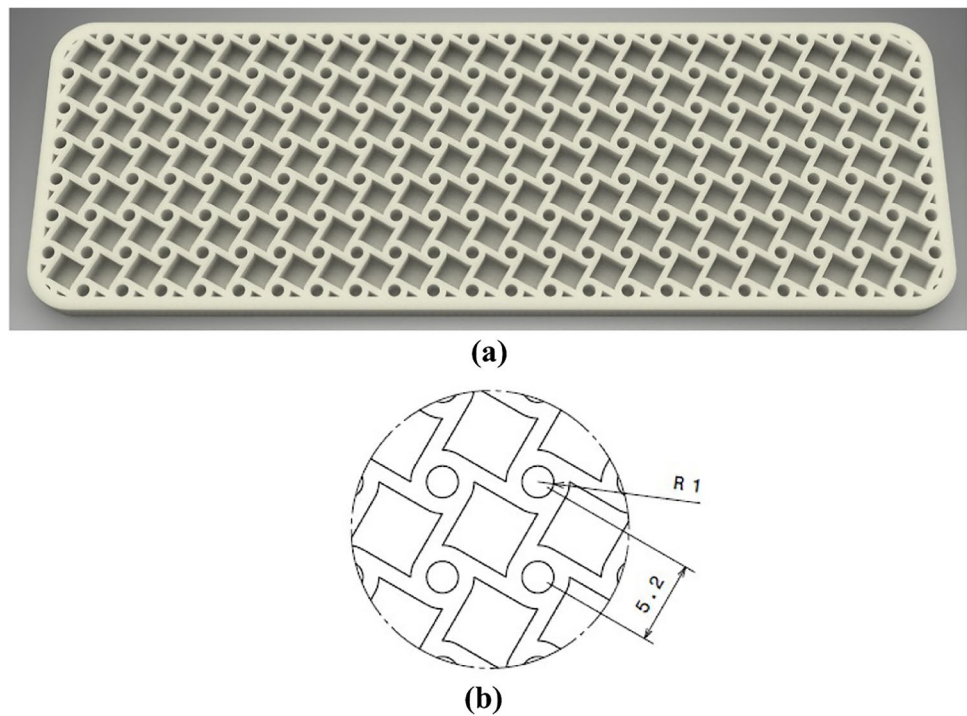


**Fig. 14** Star shapes in nature: **a** starfish; **b** white correa (a native Australian flower)



structure being designed to have a Poisson's ratio of  $-0.8$ , an NPR of  $-0.92$  was ultimately measured for minor strains [64]. The mechanical properties of the unit cell and lattice made with the arrowhead arrangement have been studied rigorously [65]. Due to the diverse advantages of the arrowhead structures [66, 67], they are employed here to assess the bending resistance of the scale model of scooter deck with a similar core design. Figures 16a and b depict the proposed bottom shell of the scale model of deck, with the arrowhead structure at its core and the dimension of the designed arrowhead unit cell, respectively.

### 3.1.5 FG arrowhead structure

Materials with FG designs are one of the most optimal options for fabricating lightweight structures due to their gradual variations in their arrangements and locally tailored properties [68, 69]. Despite their low density, they can tolerate destructive stress. Mahmoud et al. used porosity-graded lattice structures in bone implants to mimic natural bone properties [70]. Generally, in these structures, the dimension of the unit cells changes with a constant slope across the object. Magalhaes et al. observed the auxetic and tensile behaviors of braided composites [71].

Their findings reveal that compared to the material properties, structural parameters have more impact on both tensile and auxetic properties. In recent years, utilizing bamboo (see Fig. 17a) as an eco-friendly material in a broad range of engineering applications has gained increasing attention. Bamboos can be used in applications such as civil construction [73] and bridges [74] since they have an efficient combination of strength and stiffness to weight ratio, tensile strength, and fracture resistance, which are crucial for the structural design of high-strength structures under bending [73]. Bamboos consist of parenchyma cells that are located near the vascular bundles. As shown in the cross-section view in Fig. 17b, from the outside surface to the interior, the ratio of vascular bundles to parenchyma matrices decreases [75].

For this purpose, due to the fact that the maximum force acts in the middle of the scale model of deck, an FG arrowhead design inspired by a bamboo structure is devised and applied to the deck's core. The dimension of the arrowhead unit cells (Fig. 16b) expands from the center of the small-scale deck across the  $x$ -direction, as can be seen in Fig. 17c, with a constant coefficient of 1.05. In contrast, the unit-cell measurement stays unchanged along the  $y$ -axis.

**Fig. 15** **a** Star-shaped lattice core structure; **b** dimensions of the star-shaped unit cell.

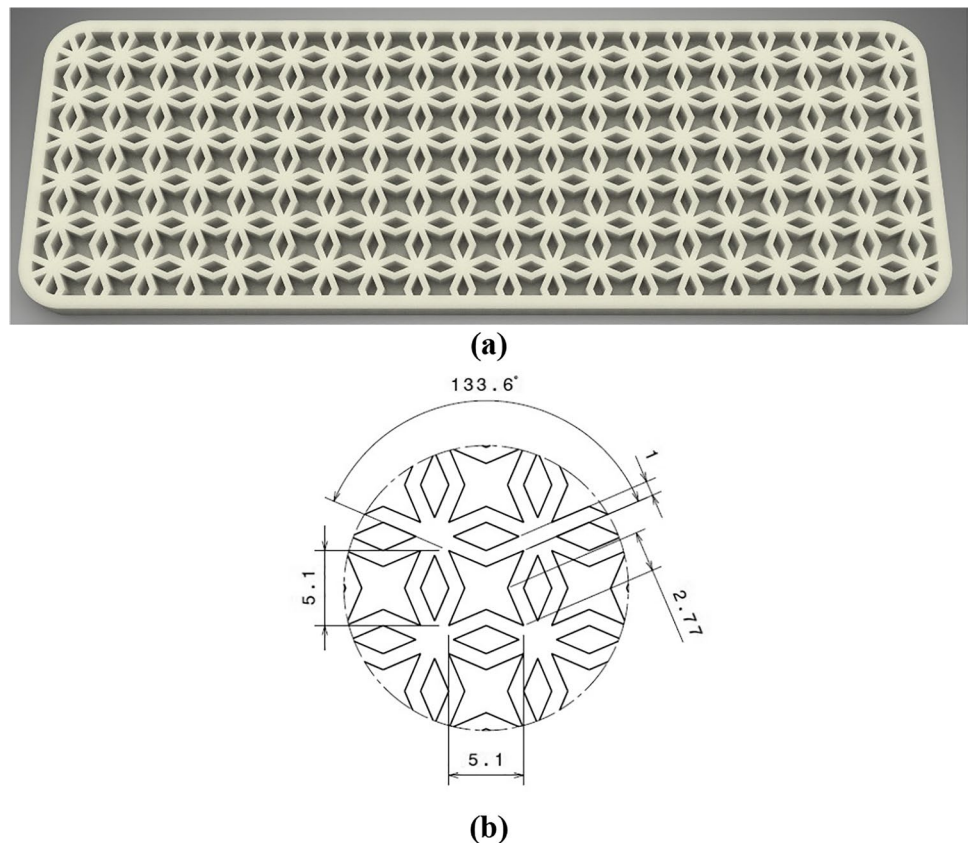


**Fig. 16** **a** Arrowhead lattice core structure; **b** dimensions of the arrowhead unit cell

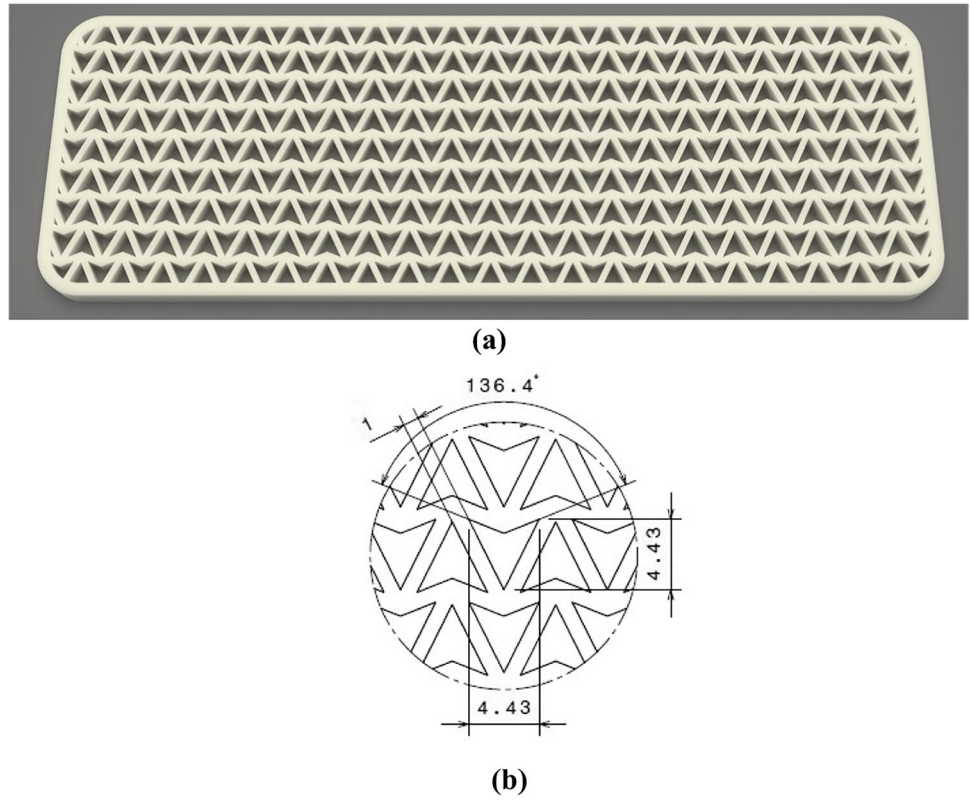
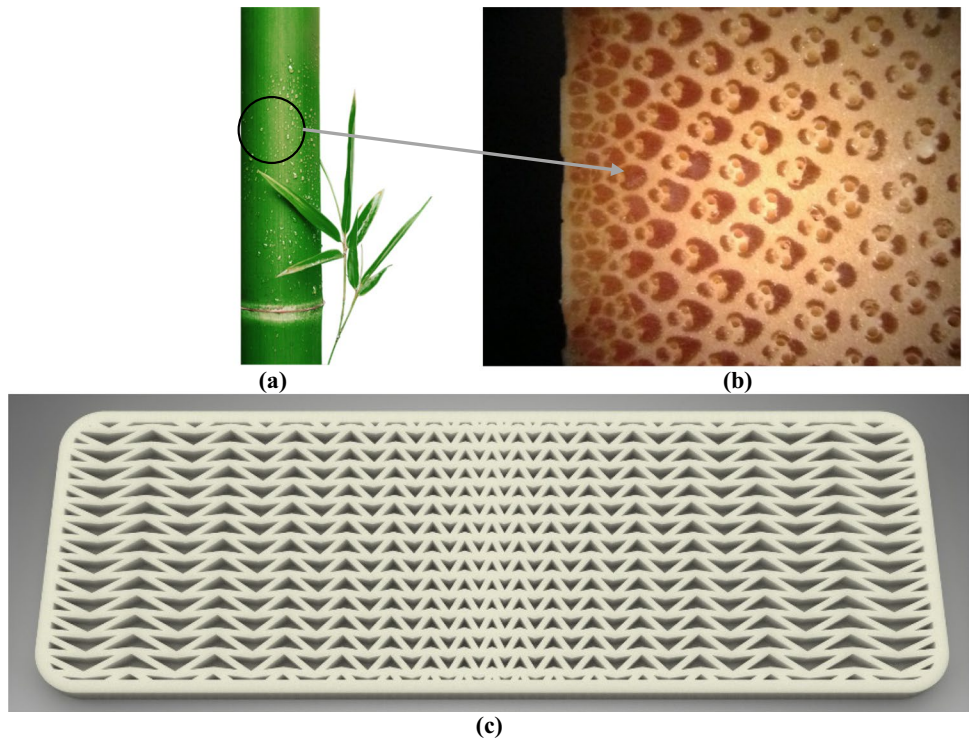


**Fig. 17** **a** Bamboos; **b** a photograph of a cross-section of a bamboo stem, the light areas are the parenchyma matrices and the dark areas are fibers [72]; **c** FG arrowhead lattice core structure



### 3.2 Mechanical behavior of the scale model of scooter deck with different core patterns

As mentioned earlier, the scale model of scooter decks designed with the core structures are subjected to a three-point bending test and simulated via the geometrically non-linear FEM software package ANSYS. Based on the loading nose, a constant displacement of 4 mm in the  $z$ -direction is applied, and the reaction force for each designed scale model of deck is determined. Figure 18 depicts a comparison of reaction force-displacement curves from the developed core designs.

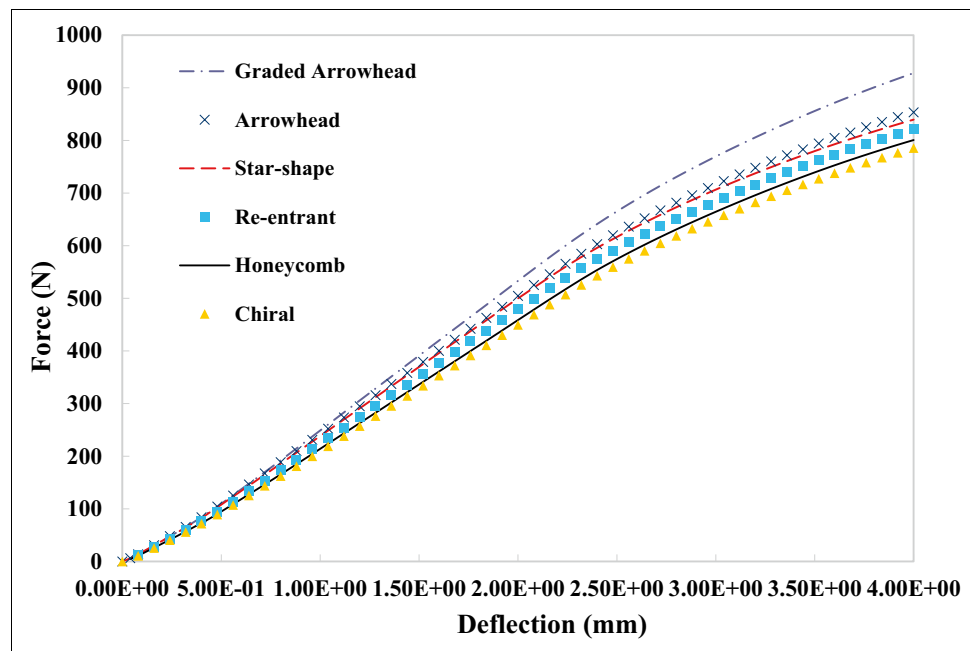
From the information provided in the figure, it is seen that all core designs result in a similar force-deflection response in the small deformation range (less than 0.1 mm). However, as the force/displacement increases, the difference in response of different designs becomes obvious. It is evident that the FG arrowhead structure can withstand the maximum forces in all deformation ranges. However, when compared to other designs, the chiral core is by far the weakest structure in terms of tolerating forces. For instance, the FG arrowhead structure withstands around 18% larger force at the final deflection value (4 mm) than the tetrachiral sample deck core, that is a substantial improvement. Considering that the highest stress occurs in the center of the small-scale deck, just underneath the load application region, the FG arrowhead design demonstrates the best bending resistance when compared to the other applied patterns. The scale model of deck with the FG arrowhead core experiences the highest force of 930 N at 4 mm. The highest force value for the remaining patterns is 854 N that is related to the uniform arrowhead design. Compared to the uniform arrowhead design, the FG

arrowhead pattern lowers the deflection in the middle of the scale model of deck by up to 14.7% for a final force of 854 N. In the real application, the weight of the rider applies a load to the center of the scale model of deck, and this load could be different depending on the riders' weight. When the mechanical behaviors of different designs are investigated in a constant force condition, the results become very interesting. Once the force reaches 785 N, the deflection in the center of the FG arrowhead deck is reduced by 30% compared to the tetrachiral design. Also, at a constant deflection of 4 mm, the FG arrowhead demonstrated an 18% improvement in force over the tetrachiral lattice structure.

## 4 Conclusion

In this paper, different bio-inspired and architected metamaterial core structures were introduced and applied to a scale model of scooter deck under a three-point bending test. A scale sample of deck with a honeycomb core was initially developed and fabricated from PLA via the FFF 3D printing technique. Its bending behavior was then investigated experimentally under the three-point bending condition. Following that, the experiment was simulated by implementing a geometrically non-linear FEM. A comparison study showed that the results of the FEM model agree well with the experimental data in small and large deformation regimes. After this validation, the bending resistance was numerically evaluated by applying various designs inspired by natural patterns and shapes to the deck's core, such as re-entrant, tetrachiral, star-shaped, arrowhead, and graded arrowhead structures. Based

**Fig. 18** Force-deflection responses for all the designed sample decks



on experimental and numerical analyses, it was found that the FG arrowhead structure enhances the bending resistance by 14.7% compared to the uniform arrowhead structure at a fixed force of 854 N. Eventually, in comparison with the tetrachiral cellular structure, at the constant force of 785 N, the FG arrowhead reduces the central deflection by 30%. Additional effort could be also considered toward lattice structures inspired from plants and tree using L-systems as recently addressed in the research work of Al Khalil et al. [76]. The presented conceptual designs and results are expected to be instrumental towards an efficient and reliable design of scooter decks with high performance and safety.

**Author contribution** Conceptual design: N.N. and M.B.  
Methodology and investigation: N.N. and M.B.  
Data collection and validation: N.N.  
Formal analysis: N.N., I.M., A.Z., F.D. and M.B.  
Discussion: I.M., A.Z., F.D. and M.B.  
Writing—first draft: N.N. and I.M.  
Writing—edit: A.Z., F.D. and M.B.  
Supervision: M.B.  
Project administration: M.B.

**Data availability** All data will be provided upon request from the corresponding author.

**Code availability** All simulation codes will be provided upon request from the corresponding author.

## Declarations

**Ethics approval** Not applicable.

**Consent to participate** Not applicable.

**Consent for publication** All authors read and approved the final manuscript for publication.

**Competing interests** The authors declare no competing interests.

**Open Access** This article is licensed under a Creative Commons Attribution 4.0 International License, which permits use, sharing, adaptation, distribution and reproduction in any medium or format, as long as you give appropriate credit to the original author(s) and the source, provide a link to the Creative Commons licence, and indicate if changes were made. The images or other third party material in this article are included in the article's Creative Commons licence, unless indicated otherwise in a credit line to the material. If material is not included in the article's Creative Commons licence and your intended use is not permitted by statutory regulation or exceeds the permitted use, you will need to obtain permission directly from the copyright holder. To view a copy of this licence, visit <http://creativecommons.org/licenses/by/4.0/>.

## References

- Shimoyama K et al (2011) Design optimization of a sport shoe sole structure by evolutionary computation and finite element method analysis. *Proc Inst Mech Eng P J Sport Eng Technol* 225(4):179–188
- Caravaggi P et al (2020) A novel cervical spine protection device for reducing neck injuries in contact sports: design concepts and preliminary in vivo testing. *Sports Biomech* 19(3):382–394
- Gudimelta P, Kelson N, El-Atm B (2009) Analysis of the hydrodynamic performance of three- and four-fin surfboards using computational fluid dynamics. *Aust J Mech Eng* 7(1):61–67
- Mosleh Y et al (2018) Designing safer composite helmets to reduce rotational accelerations during oblique impacts. *Proc Inst Mech Eng* 232(5):479–491
- Sakellariou K, Rana ZA, Jenkins KW (2017) Optimisation of the surfboard fin shape using computational fluid dynamics and genetic algorithms. *Proc Inst Mech Eng P J Sport Eng Technol* 231(4):344–354
- Penta F et al (2018) Low-velocity impacts on a polymeric foam for the passive safety improvement of sports fields: meshless approach and experimental validation. *Appl Sci* 8(7):1174
- Mesicek J et al (2021) Comprehensive view of topological optimization scooter frame design and manufacturing. *Symmetry* 13(7):1201
- Aizpuru M et al (2019) Motorized scooter injuries in the era of scooter-shares: a review of the national electronic surveillance system. *Am J Emerg Med* 37(6):1133–1138
- Meraghni F, Desrumaux F, Benzeggagh M (1999) Mechanical behaviour of cellular core for structural sandwich panels. *Compos A: Appl Sci Manuf* 30(6):767–779
- He M, Hu W (2008) A study on composite honeycomb sandwich panel structure. *Mater Des* 29(3):709–713
- Plątek P et al (2019) Investigation on deformation process of cellular structures with gradient topology manufactured additively. In: *AIP Conference Proceedings*. AIP Publishing LLC
- Compton BG, Lewis JA (2014) 3D printing: 3d-printing of light-weight cellular composites (*Adv. Mater.* 34/2014). *Adv Mater* 26(34):6043–6043
- Bodaghi M et al (2017) Large deformations of soft metamaterials fabricated by 3D printing. *Mater Des* 131:81–91
- Saxena KK, Das R, Calius EP (2016) Three decades of auxetics research— materials with negative Poisson's ratio: a review. *Adv Eng Mater* 18(11):1847–1870
- van Hecke KMMG (2019) M Wegener M 3d metamaterials. *Nat Rev Phys* 1(3):198
- Lakes R (1993) *Advances in negative Poisson's ratio materials*. Wiley Online Library
- Najafi M, Ahmadi H, Liaghat G (2022) Evaluation of the mechanical properties of fully integrated 3D printed polymeric sandwich structures with auxetic cores: experimental and numerical assessment. *Int J Adv Manuf Technol* 122(9):4079–4098
- Zhai Z, Wang Y, Jiang H (2018) Origami-inspired, on-demand deployable and collapsible mechanical metamaterials with tunable stiffness. *Proc Natl Acad Sci* 115(9):2032–2037
- Dudek K et al (2018) Negative and positive stiffness in auxetic magneto-mechanical metamaterials. *Proc Math Phys Eng* 474(2215):20180003
- Babae S et al (2013) 3D soft metamaterials with negative Poisson's ratio. *Adv Mater* 25(36):5044–5049
- Zadpoor AA (2016) Mechanical meta-materials. *Mater Horiz* 3(5):371–381
- Shah J et al (2019) Large-scale 3D printers for additive manufacturing: design considerations and challenges. *Int J Adv Manuf Technol* 104(9):3679–3693
- Ngo TD et al (2018) Additive manufacturing (3D printing): a review of materials, methods, applications and challenges. *Compos Part B Eng* 143:172–196
- McWilliams A (2015) Global markets for 3-D printing. *BCC Research, Massachusetts Fig.* p 16

25. Haghghi A, Li L (2018) Study of the relationship between dimensional performance and manufacturing cost in fused deposition modeling. *Rapid Prototyp J* 24(2):395–408
26. Shahrubudin N, Lee TC, Ramlan R (2019) An overview on 3D printing technology: technological, materials, and applications. *Procedia Manuf* 35:1286–1296
27. Bak D (2003) Rapid prototyping or rapid production? 3D printing processes move industry towards the latter. *Assem Autom* 23(4):340–345
28. Berman B (2012) 3-D printing: the new industrial revolution. *Bus Horiz* 55(2):155–162
29. Lin C, Chua C, Yeo J (2013) Design of high performance badminton shuttlecocks: virtual and rapid prototyping approach: this paper reports a shuttlecock design whose performance exceeded existing commercial products. *Virtual Phys Prototyp* 8(2):165–171
30. Lee H, Eom R-I, Lee Y (2016) Development of ergonomic leg guard for baseball catchers through 3D modeling and printing. *J Fash Bus* 20(3):17–29
31. Novak J, Burton D, Crouch T (2019) Aerodynamic test results of bicycle helmets in different configurations: towards a responsive design. *Proc Inst Mech Eng P J Sport Eng Technol* 233(2):268–276
32. Harte D, Paterson A (2018) The fastest field sport in the world: a case report on 3-dimensional printed hurling gloves to help prevent injury. *J Hand Ther* 31(3):398–410
33. Amorim DJN, Nachtigall T, Alonso MB (2019) Exploring mechanical meta-material structures through personalised shoe sole design. *Proceedings of the ACM symposium on computational fabrication*. pp 1–8
34. Nessi A, Stanković T (2018) Topology, shape, and size optimization of additively manufactured lattice structures based on the superformula. In: *International Design Engineering Technical Conferences and Computers and Information in Engineering Conference*. American Society of Mechanical Engineers
35. Soltani A et al (2020) 3D printing on-water sports boards with bio-inspired core designs. *Polymers* 12(1):250
36. Gately RD et al (2017) Additive manufacturing, modeling and performance evaluation of 3D printed fins for surfboards. *MRS Adv* 2(16):913–920
37. Park J-H, Goo B, Park K (2019) Topology optimization and additive manufacturing of customized sports item considering orthotropic anisotropy. *Int J Precis Eng* 20(8):1443–1450
38. Cazón-Martín A et al (2019) Design and manufacturing of shin pads with multi-material additive manufactured features for football players: a comparison with commercial shin pads. *Proc Inst Mech Eng P J Sport Eng Technol* 233(1):160–169
39. Balaguru S et al (2019) Structural and modal analysis of scooter frame for design improvement. *Mater Today: Proc* 16:1106–1116
40. Chou J-R, Hsiao S-W (2005) Product design and prototype making for an electric scooter. *Mater Des* 26(5):439–449
41. Koontz AM et al (2010) Design features that affect the maneuverability of wheelchairs and scooters. *Arch Phys Med Rehabil* 91(5):759–764
42. Murariu M, Dubois P (2016) PLA composites: from production to properties. *Adv Drug Deliv Rev* 107:17–46
43. Wen H-M, Jones N (1993) Experimental investigation of the scaling laws for metal plates struck by large masses. *Int J Impact Eng* 13(3):485–505
44. Hamada H, Ramakrishna S (1995) Scaling effects in the energy absorption of carbon-fiber/PEEK composite tubes. *Compos Sci Technol* 55(3):211–221
45. Tarfaoui M et al (2007) Scale and size effects on dynamic response and damage of glass/epoxy tubular structures. *J Compos Mater* 41(5):547–558
46. Kashani MH et al (2015) Investigation of scaling effects on fiber metal laminates under tensile and flexural loading. *Proc Inst Mech Eng* 229(3):189–201
47. Bates SRG, Farrow IR, Trask RS (2016) 3D printed polyurethane honeycombs for repeated tailored energy absorption. *Mater Des* 112:172–183
48. Li T, Wang L (2017) Bending behavior of sandwich composite structures with tunable 3D-printed core materials. *Compos Struct* 175:46–57
49. Aziz A et al (2021) Geometrical scaling effects in the mechanical properties of 3d-printed body-centered cubic (BCC) lattice structures. *Polymers* 13:3967
50. Standard A (2003) Standard test method for tensile properties of plastics. *ASTM International Designation: D 638:1–13*
51. Guo X et al (2015) Influence of strain rates on the mechanical behaviors of shape memory polymer. *Smart Mater Struct* 24(9):095009
52. Robert F (1985) An isotropic three-dimensional structure with Poisson's ratio = -1. *J Elast* 15:427–430
53. Alomarah A et al (2017) Mechanical properties of the 2D reentrant honeycomb made via direct metal printing. In: *IOP Conference Series: Materials Science and Engineering*. IOP Publishing
54. Boldrin L et al (2016) Dynamic behaviour of auxetic gradient composite hexagonal honeycombs. *Compos Struct* 149:114–124
55. Namvar N et al (2022) Reversible energy absorption of elastoplastic auxetic, hexagonal, and AuxHex structures fabricated by FDM 4D printing. *Smart Mater Struct* 31(5):055021
56. Prall D, Lakes RS (1997) Properties of a chiral honeycomb with a Poisson's ratio of -1. *Int J Mech Sci* 39(3):305–314
57. Thomson BK, Thomson W (2010) *Baltimore lectures on molecular dynamics and the wave theory of light*. Cambridge University Press
58. Scarpa F et al (2007) Elastic buckling of hexagonal chiral cell honeycombs. *Compos A: Appl Sci Manuf* 38(2):280–289
59. Li H et al (2017) In plane mechanical properties of tetrachiral and antitetrachiral hybrid metastructures. *J Appl Mech* 84(8)
60. Qi C et al (2019) In-plane crushing response of tetra-chiral honeycombs. *Int J Impact Eng* 130:247–265
61. Grima JN et al (2005) On the potential of connected stars as auxetic systems. *Mol Simul* 31(13):925–935
62. Gong X et al (2015) Zero Poisson's ratio cellular structure for two-dimensional morphing applications. *Compos Struct* 134:384–392
63. Liu H-T, Wang L (2022) Design 3D improved star-shaped honeycomb with different tip angles from 2D analytical star-shaped model. *Compos Struct* 283:115154
64. Larsen UD, Signund O, Bouwsta S (1997) Design and fabrication of compliant micromechanisms and structures with negative Poisson's ratio. *J Microelectromech Syst* 6(2):99–106
65. Brighenti R et al (2016) Nonlinear deformation behaviour of auxetic cellular materials with re-entrant lattice structure. *Fatigue Fract Eng Mater Struct* 39(5):599–610
66. Li X et al (2019) Novel auxetic structures with enhanced mechanical properties. *Extreme Mech Lett* 27:59–65
67. Boopathi B, Ponniah G, Burela RG (2020) Realizing the impact and compressive strengths of an arrowhead auxetic structure inspired by topology optimization. *Int J Adv Eng Sci Appl Math* 12(3):211–217
68. Loh GH et al (2018) An overview of functionally graded additive manufacturing. *Addit Manuf* 23:34–44
69. Ma X et al (2022) Mechanical and energy absorption properties of functionally graded lattice structures based on minimal curved surfaces. *Int J Adv Manuf Technol* 118(3):995–1008
70. Mahmoud D, Elbestawi M (2019) Selective laser melting of porosity graded lattice structures for bone implants. *Int J Adv Manuf Technol* 100(9):2915–2927
71. Magalhaes R et al (2016) Development, characterization and analysis of auxetic structures from braided composites and study the influence of material and structural parameters. *Compos A: Appl Sci Manuf* 87:86–97
72. Crutcher, R. Timber bamboo cross-section. Available online: <http://www.microlabgallery.com/gallery/Bamboo%20Macro%201.aspx> (accessed on 5 December 2019).

73. Ghavami K (2005) Bamboo as reinforcement in structural concrete elements. *Cem Concr Compos* 27(6):637–649
74. Xiao Y, Zhou Q, Shan B (2010) Design and construction of modern bamboo bridges. *J Bridge Eng* 15(5): 533–541
75. Osorio L et al (2018) In-depth study of the microstructure of bamboo fibres and their relation to the mechanical properties. *J Reinf Plast Compos* 37(17):1099–1113
76. Al Khalil M, Belkebir H, Lebaal N, Demoly F, Roth S. (2022) A Biomimetic Design Method for 3D-Printed Lightweight Structures Using L-Systems and Parametric Optimization. *Appl Sci* 12(11):5530. <https://doi.org/10.3390/app12115530>

**Publisher's note** Springer Nature remains neutral with regard to jurisdictional claims in published maps and institutional affiliations.